



Thermal studies of Mn²⁺-doped ZnO powders formation by sol–gel method

Cristina Maria Vladut¹ · Susana Mihaiu¹ · Oana Cătălina Mocioiu¹ · Irina Atkinson¹ · Jeanina Pandeale-Cusu¹ · Elena Maria Anghel¹ · Jose Maria Calderon-Moreno¹ · Maria Zaharescu¹

Received: 18 December 2017 / Accepted: 29 July 2018 / Published online: 14 August 2018
© Akadémiai Kiadó, Budapest, Hungary 2018

Abstract

In the present contribution, the study of nanostructured powders of Mn²⁺-doped ZnO with different doping concentration (1, 2, 5 at%) was approached. The samples were synthesized by sol–gel method, and the influence of the Mn content on the thermal behavior of the resulted gels was established by thermogravimetric and thermodifferential analysis. Based on the results obtained by thermal analysis, the gels were isothermally treated at 500 °C, 1 h. The XRD powder measurements revealed that all samples had hexagonal wurtzite structure and no other secondary phases were observed suggesting that the Mn²⁺ ions have substituted Zn sites. Moreover, the incorporation of Mn²⁺ into ZnO lattice was also confirmed by Infrared and Raman spectroscopy. Energy-dispersive X-ray analysis indicates the existence of Mn²⁺ in all samples, even in that with 1 at% Mn. The morphology of the samples depends on Mn²⁺ concentrations. A decrease in the grain size with the increase in Mn²⁺ concentration was observed. Mn²⁺-doped ZnO nanopowders with desired structure and properties as promising materials in potential piezoelectric applications, were obtained.

Keywords Mn-doped ZnO powders · Sol–gel method · Thermal behavior

Introduction

Zinc oxide (ZnO) is a wide band gap semiconductor exhibiting *n*-type conductivity with wide energy band gap (3.36 eV at room temperature). Furthermore, ZnO is abundant in nature, nontoxic, chemically and mechanically stable and has tunable band gap, high transparency and piezoelectric behavior. Based on these properties, ZnO is a promising candidate for applications like transparent electrode for solar cell, flat panel devices, organic light emitting diode, thin-film transistor–liquid crystal display (TFT–LCD), gas sensors, piezoelectric nanogenerators [1–5].

Depending on the required properties and applications, the properties of ZnO can be improved by doping with different ions. The dopant added into the ZnO nanostructure influences the band gap, as well as the electrical and optical properties of ZnO [6–9]. Among all dopants, Mn²⁺ is one of the most encouraging because the first half of the d-band is occupied, creating a stable fully polarized state, and it has higher resistivity and the highest magnetic moment [10]. As a consequence of similar radii of Zn²⁺ (0.074 nm) and Mn²⁺ (0.080 nm), the manganese ion can easily be incorporated into ZnO lattice without altering its original structure [11]. The band gap values were found to gradually decrease from 3.06 eV for ZnO to 2.83 eV for ZnO doped with 7% Mn [8].

The Mn²⁺-doped ZnO system is studied because of its advantages as high magnetic moments at room temperature and high thermal solubility. ZnO and Mn²⁺-doped ZnO can be prepared by different methods such as solid-state reaction [12], high-temperature hydrolytic process [13], pulsed laser deposition [14], ion implantation [15], RF magnetron sputtering [16], molecular beam epitaxy [17], precipitation [18, 19], spray pyrolysis [20] and sol–gel method [21–31].

✉ Cristina Maria Vladut
vladut@icf.ro

✉ Oana Cătălina Mocioiu
omocioiu@icf.ro

¹ Institute of Physical Chemistry, “Ilie Murgulescu” of the Romanian Academy, 202 Splaiul Independentei, 060021 Bucharest, Romania

However, the existent experimental magnetism results of Mn^{2+} -doped ZnO are very controversial. Due to different preparation conditions and post-synthetic treatment, various magnetisms have been reported, such as ferromagnetism [13, 32, 33] antiferromagnetism [15, 34, 35], spin glass behavior [12, 36] and paramagnetism [16, 37].

In the present work, ZnO and Mn^{2+} -doped ZnO-based gels and nanostructured powders with different manganese concentration (1, 2, 5 at%) were studied.

The samples were synthesized by sol–gel method, and the influence of the manganese content on the thermal behavior of resulted gels was established by thermogravimetric and differential thermal analysis (TG/DTA).

Based on the results obtained, the adequate thermal treatment of the gels was selected in order to obtain Mn^{2+} -doped ZnO nanopowders with desired structure and properties as promising materials in potential piezoelectric applications.

It has to be mention that in the previous research papers on Mn^{2+} -doped ZnO prepared by sol–gel method [21–31], different precursors were used and the thermal behavior was not approached.

Experimental

Materials

Zinc acetate dihydrate— $\text{Zn}(\text{CH}_3\text{COO})_2 \cdot 2\text{H}_2\text{O}$ (Merck), and anhydrous manganese acetate— $\text{Mn}(\text{CH}_3\text{COO})_2$ (Merck), were used as source of zinc and manganese, respectively, and absolute ethanol— $\text{C}_2\text{H}_5\text{OH}$ (Emsure), and methanol CH_3OH (Merck), as solvents and triethanolamine— $\text{C}_6\text{H}_{15}\text{NO}_3$ (TEA, Merck), as stabilizer. All reagents used in the experiments were of analytical grade.

Methods

Samples preparation

Precursor solutions of 0.1 M ZnO and Mn^{2+} -doped ZnO were obtained through sol–gel method. Zinc acetate dihydrate was dissolved in ethanol and homogenized at 50 °C for 1 h. During the homogenization, TEA was added drop by drop. The molar ratio between zinc acetate and triethanolamine was 5:1.

In order to obtain 0.1 M precursor solution of Mn, anhydrous manganese acetate was dissolved in methanol. For 1 at%, 2 at%, 5 at% Mn-doped ZnO, adequate quantities were added in the Zn solution. The mixture was stirred at 50 °C for 1 h to yield a clear and homogenous

solution. The solutions were left for gelling at room temperature for 7 days, and opaque gels were obtained.

Based on the results obtained by thermal analysis, the samples were thermally treated at 500 °C for 1 h, with a heating rate of 5 °C min^{-1} .

Methods of characterization

The thermal behavior of the synthesized gels was determined by differential thermal analysis and thermogravimetric analysis using Mettler Toledo TG/DTA 851e equipment in Al_2O_3 crucibles and in flowing air atmosphere. The maximum temperature was set at 1000 °C, and the heating rate was of 5 °C min^{-1} .

FTIR spectra for gels and powders were recorded with a Nicolet 6700 apparatus in 400–4000 cm^{-1} domain. The powders were immobilized in KBr pellets, and the spectra were recorded in transmittance mode. The sensitivity of measurements was of 4 cm^{-1} .

Sample morphology was characterized by scanning electron microscopy (SEM) using a high-resolution microscope, FEI Quanta3 DFEG model, at an accelerating voltage of 5 kV, in high-vacuum mode with Everhart–Thornley secondary electron (SE) detector coupled with energy-dispersive X-ray (EDX) analysis. The apparatus program was used for the grain size calculation.

X-ray diffraction experiments were performed by using a Rigaku Ultima IV diffractometer in parallel beam geometry equipped with $\text{CuK}\alpha$ radiation (wavelength 1.5406 Å) operating at 40 kV and 30 mA. The XRD patterns were collected in 2θ range between 10 and 80 with a speed of 2° min^{-1} and a step size of 0.02°. PDXL software from Rigaku, connected to ICDD database, was used for phase identification and lattice parameters calculation using whole-powder-pattern fitting method (WPPF). The diffraction peak profiles were modeled by a split-pseudo-Voigt function and B-spline background model. Crystallite size along (101) direction has been calculated using Scherer's equation:

$$D = \frac{k \cdot \lambda}{(\text{FWHM}) \cdot \cos \theta} \quad (1)$$

where D is crystallite size, λ is wavelength of the Cu $\text{K}\alpha$ radiation (1.54056 Å), FWHM is full width at half maximum, θ is Bragg's diffraction angle and k is the shape factor taken as 0.9.

Micro-Raman spectra were recorded by means of a Jobin–Yvon–Horiba LabRam HR 800 spectrometer equipped with a Nd:YAG (532 nm) laser line and a x50LWD/0.55 NA air objective. Spot diameters of ~ 1.1 mm on the sample surface provided a spectral resolution better than 2 cm^{-1} . Local heating effect was avoided by using a laser power up to 2 mW.

Results and discussion

As-prepared samples

As mentioned above, in the experimental conditions used in the present work, opaque quasi-crystalline gels were obtained. Our previous papers regarding the preparation of ZnO nanoparticles have shown that the corresponding gel was a mixture of different Zn-based phases as hydrozincite and zinc acetate dihydrate [38].

FTIR characterization of the samples

The spectrum of as-prepared ZnO-based sample presents the bands in 3600–2500 cm⁻¹ region characteristic to vibration of C–H, NH and O–H bonds. The small bands at 2972, 2867 cm⁻¹ are characteristic to vibrations of C–H bond in CH₃ groups. The bands are shifted from their position in zinc acetate spectrum [38] probably due to formation of zinc hydroxyacetate. The carboxyl bands (asymmetric and symmetric stretching of C=O, respectively) occur in the FTIR spectra in the 1400–1580 cm⁻¹ range and ν C–O at 1070 cm⁻¹ [38]. The bands below 686 cm⁻¹ are due to Zn–O vibration [38, 39].

The FTIR spectra of the Mn²⁺-doped ZnO samples show the characteristic bands of the C–H and O–H bonds in 3600–2500 cm⁻¹ region, also. The bands of 1582 cm⁻¹ and 1418 cm⁻¹ are characteristic of the C=O bond in the COO⁻ group and those of 1077 cm⁻¹ and 1045 cm⁻¹ are assigned to C–O bond [38]. In the wavelength range of 500–700 cm⁻¹, the bands characteristic of the Zn–O bond is present. The bands at 421 cm⁻¹ and 408 cm⁻¹ are characteristic of the Mn–O bond as was reported in the literature [40].

Based on observation of shifted positions of bands in the FTIR spectra, we can assume that during the gelation process a zinc hydroxyacetate gel similar to structure with the one reported by Moezzi [41] was obtained (Fig. 1).

TG/DTA characterization of the samples

The TG/DTA curves of the ZnO sample are shown in Fig. 2. As stated before [38], the first two endothermic effects at 66 and 133 °C, respectively, are assigned to the elimination of ethanol and water and the effect at 215 °C could be related to the structural hydroxyl elimination. The decomposition of the Zn hydroxyacetate takes place at 297 °C accompanied by the oxidation of resulted CO to CO₂. The overlapping of the endothermic effect assigned to the gel decomposition with the exothermic one assigned to oxidation of resulted CO to CO₂ explains the small exothermic peak at 313 °C. The exothermic process at

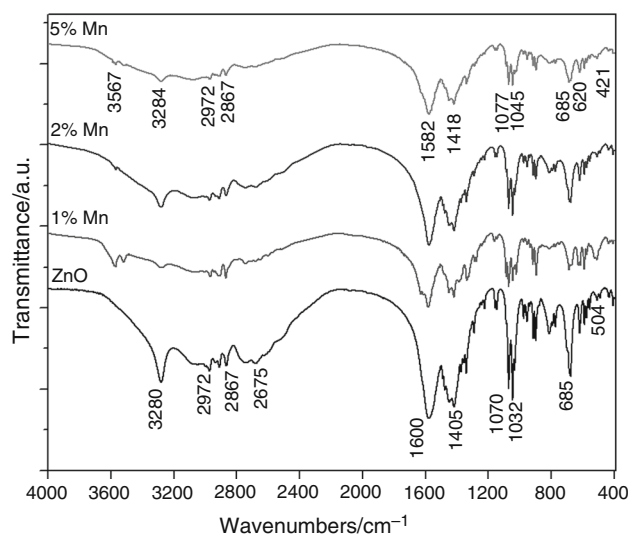


Fig. 1 FTIR of the as-prepared samples

around 428 °C may be assigned to the combustion of organic component and crystallization of ZnO from the studied gel. After 500 °C, TG curve remains constant suggesting that a thermal treatment at this temperature is enough to obtain ZnO.

The mechanism of thermal decomposition of the ZnO-based gel was previously presented and discussed [38].

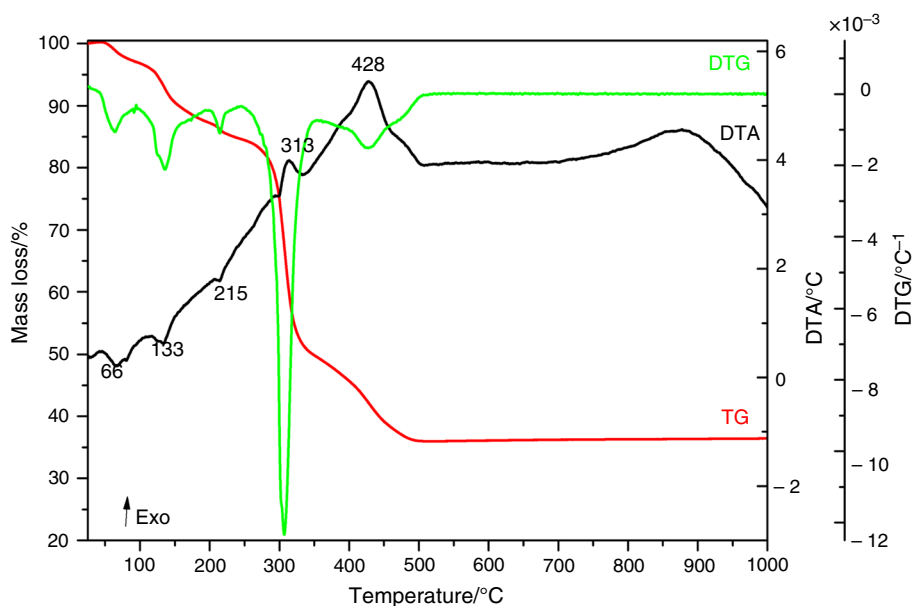
In the case of Mn²⁺-doped ZnO samples, there is a similar thermal behavior for all the studied compositions. The first two endothermic effects on the thermal analysis curve are assigned to the elimination of both ethanol and water. The zinc and manganese complex hydroxyacetate is decomposed at around 300 °C, similarly with the Zn hydroxyacetate gel. The exothermic effect from above 420 °C is attributed to the oxidation of the organic residues as well as to the crystallization of Mn²⁺-doped ZnO (Fig. 3).

For the sample containing 5% Mn²⁺, the thermal effects of the decomposition step at lower temperatures have lower intensity, while the decomposition of the sample at 422 °C is much more pronounced. This may be attributed to the formation of more thermally stable complexes by the reactions in the precursor solutions due to the presence of Mn²⁺ in a larger quantity.

The samples exhibited larger mass loss than the undoped sample (pure ZnO based gel) which indicates a higher amount of organics in the gel composition.

Due to similar thermal behavior of the undoped ZnO and Mn²⁺-doped ZnO precursor gels, the same mechanism of decomposition could be assigned.

Fig. 2 TG/DTA of the undoped ZnO sample



Thermally treated samples

Based on the results obtained by thermal analysis, the samples were thermally treated at 500 °C for 1 h, with a heating rate of 5 °C min⁻¹. The structure and the morphology of the resulted powders were investigated by SEM and EDX, FTIR, XRD and Raman spectroscopy.

SEM characterization of the powders

Figure 4 shows the SEM images of the Mn²⁺-doped ZnO samples. The images clearly indicate that similar morphology of the powders was obtained, but the grain size decreased with the Mn²⁺ concentrations. The powders consist in particles with hexagonal cross section, having a variable length between 30 and 300 nm. EDX analysis provides the composition of the samples and puts in evidence the existence of Mn²⁺ in all samples, even at those with 1% Mn.

FTIR characterization of the powders

In the FTIR spectra of the powders treated at 500 °C, the bands characteristic to organic species were not identified due to the decomposition and oxidation of the organic part during thermal treatment. The results are in good agreement with TG/DTA data, in which there are no mass losses and thermal effects after 500 °C. In Fig. 5, the spectra in 1600–400 cm⁻¹ range are presented. In the spectrum of ZnO, the bands characteristic to Zn–O–Zn vibrations were identified at 433 and 505 cm⁻¹ confirming the wurtzite structure [38]. The FTIR spectra of Mn-doped ZnO samples exhibit a broadband in the 400–600 cm⁻¹ range

assigned to formation of ZnO. In the literature, the vibration bands for Mn–O are reported at 431 cm⁻¹, 418 cm⁻¹ and 408 cm⁻¹ [40]. The maximum of the band appears in all doped samples at 421 cm⁻¹ and can be assigned to formation of Mn–O–Zn bonds. The intensity of this band decreases from the ZnO with 5% Mn to ZnO with 2% Mn and can be correlated with the crystallinity of doped powders. Mihaiu et al. [38] reported bands with maximum above 429 cm⁻¹ when ZnO was doped with Li or co-doped with Ni and Li.

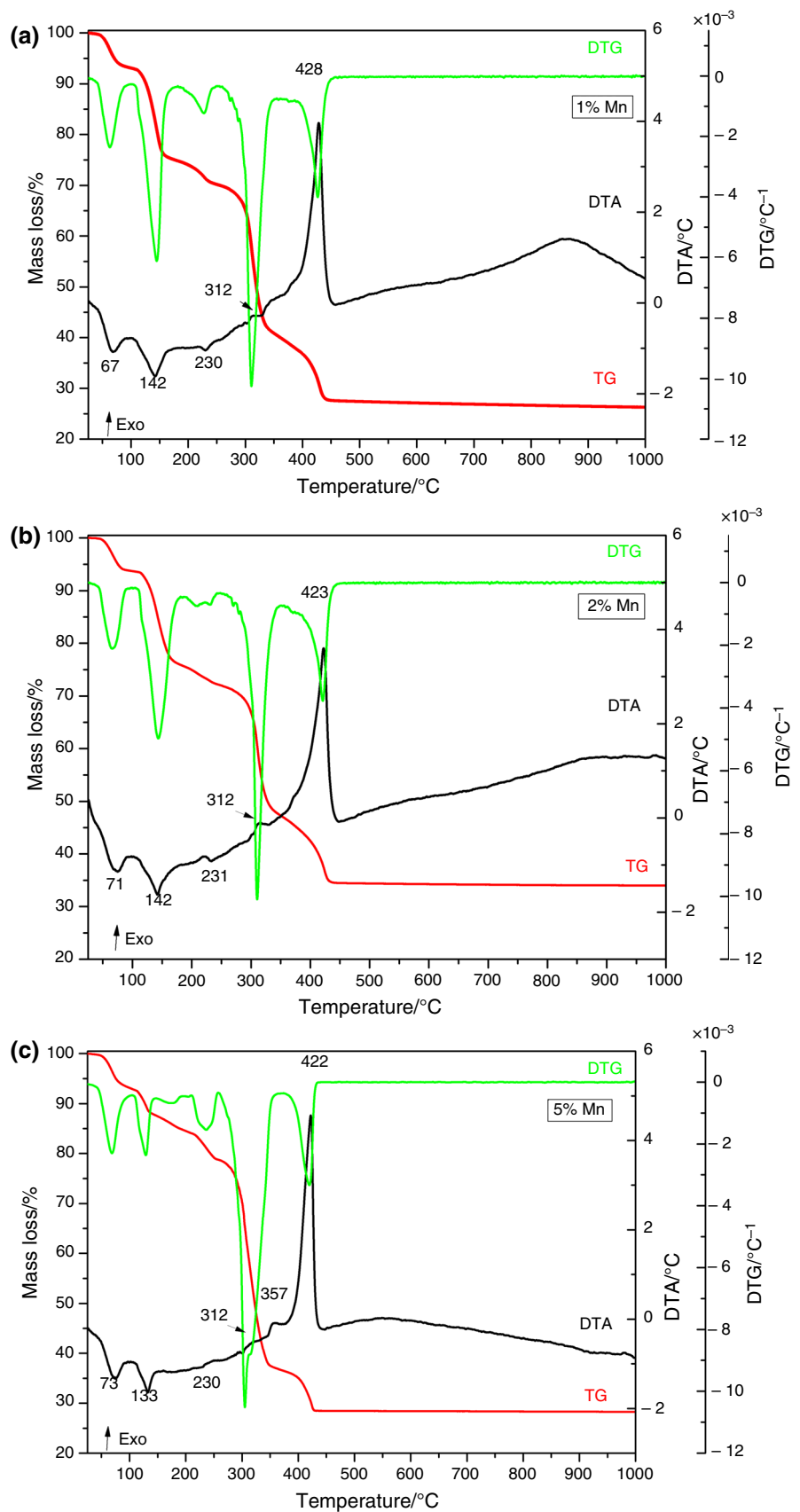
XRD characterization of powders

Figure 6 shows the XRD patterns of pure ZnO and 1 at%, 2 at% and 5 at% Mn-doped ZnO powders. All the diffraction peaks are indexed as hexagonal wurtzite structure (space group P63mc) ZnO with lattice parameters $a = b = 3.249$ Å and $c = 5.206$ Å, in good agreement with JCPDS card no. 36-1451.

In addition, the high intensity of the diffraction lines suggests the high crystalline nature of the prepared samples. No signals arising from Mn oxides or any Mn-related phases were detected on the XRD patterns indicating that the Mn²⁺ ions have probably substituted Zn sites. Previously, Hossin and Askan [42] have also reported that the manganese ions have substituted the zinc ions without changing the wurtzite structure of zinc oxide.

The calculated lattice parameters are listed in Table 1, together with the estimated standard deviation (in brackets). The values of crystallite size and FWHM along (101) direction of pure ZnO and Mn²⁺-doped ZnO samples are also given in Table 1.

Fig. 3 TG/DTA of the Mn²⁺-doped ZnO: **a** 1% Mn, **b** 2% Mn, **c** 5% Mn



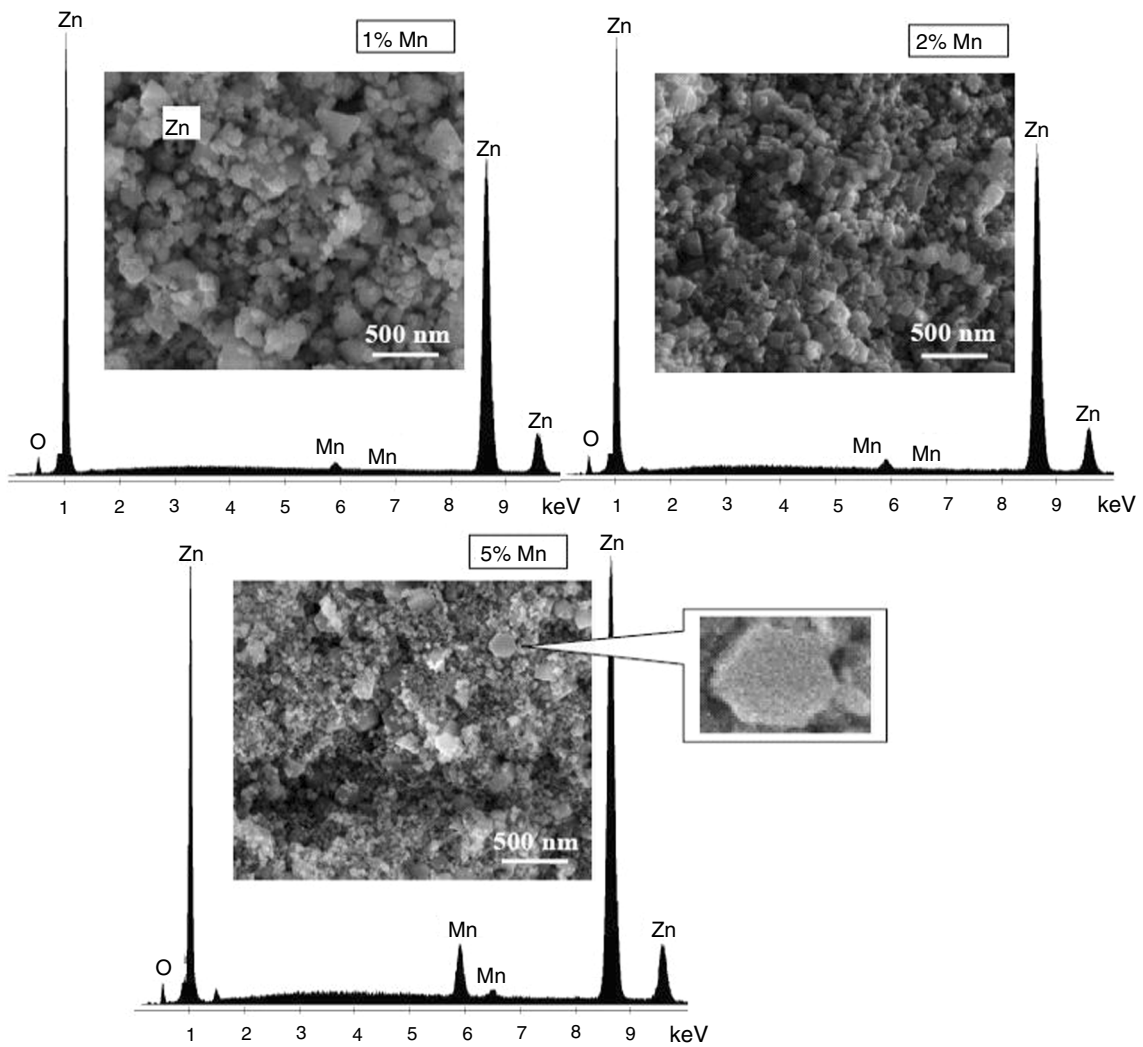


Fig. 4 SEM/EDX images of the ZnO doped with Mn²⁺ (1, 2 and 5%)

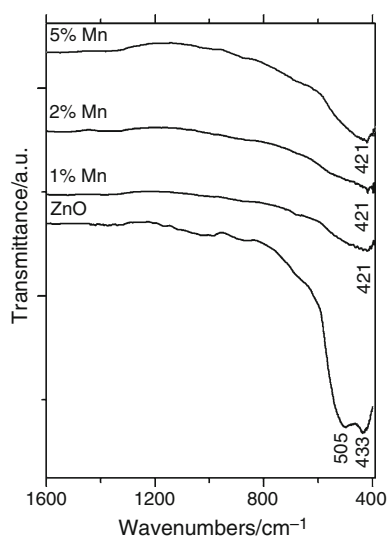


Fig. 5 FTIR spectra of the ZnO and Mn²⁺-doped ZnO powders thermally treated at 500 °C

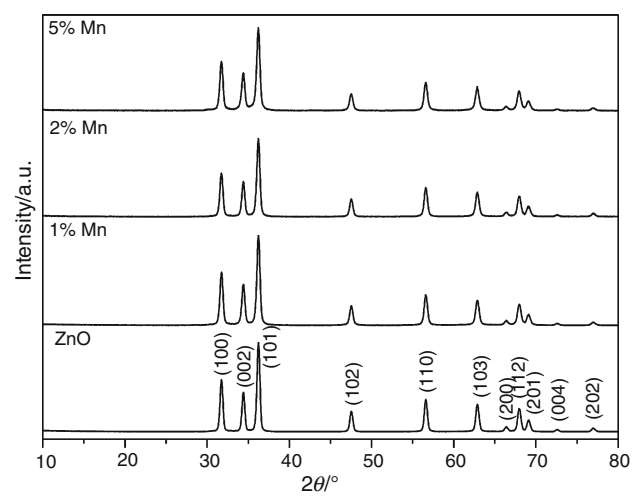


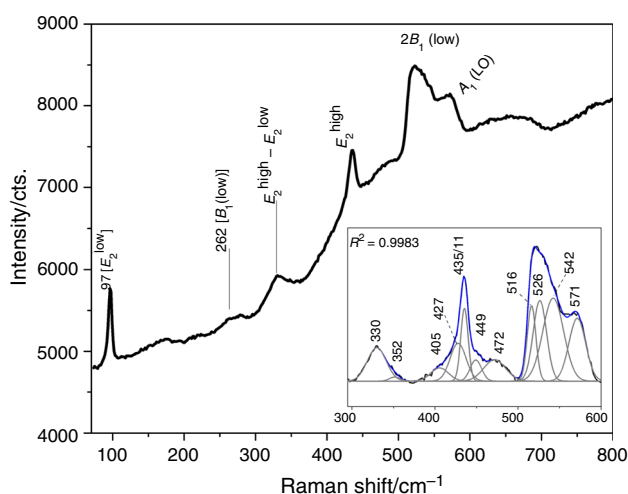
Fig. 6 XRD patterns of the ZnO and Mn²⁺-doped ZnO powders thermally treated at 500 °C

Table 1 The 2θ and FWHM values, d -spacing, crystallite size D , lattice parameters (a , c), volume V of unit cell of pure ZnO and Mn-doped ZnO powders thermally treated at 500 °C

Sample	2θ (101)	$d/\text{\AA}$	FWHM ₁₀₁ /°	$D/\text{\AA}$	$a = b/\text{\AA}$	$c/\text{\AA}$	$V/\text{\AA}^3$
ZnO	36.2333	2.4772	0.3699	236 (1)	3.2496 (2)	5.2057 (3)	47.61
1% Mn	36.2140	2.4784	0.4156	210 (1)	3.2518 (3)	5.2080 (2)	47.69
2% Mn	36.2086	2.4788	0.4158	209 (1)	3.2522 (6)	5.2070 (14)	47.70
5% Mn	36.1966	2.4796	0.4273	204 (1)	3.2524 (6)	5.2086 (13)	47.72

The increase seen in the lattice parameters as well as the volume of unit cell in the Mn²⁺-doped ZnO samples can be attributed to the fact that substitution of Mn²⁺ (ionic radius 0.8 Å) for Zn²⁺ (ionic radius 0.74 Å) requires a local expansion of the lattice to accommodate the Mn²⁺ ion in the ZnO structure [43].

A careful analysis of the XRD peak positions indicates a minor shift of the main diffraction peak (101) of the doped samples toward lower 2θ values as the concentration of Mn increased (see Table 1). This is proof of the successful incorporation of Mn²⁺ into the ZnO lattice. Moreover, an increase in the d -spacing values corresponding to (101) plane has been observed due to the shift in 2θ for the Mn-doped samples. The average crystallite size was about 236 Å for pure ZnO. A decrease in crystallite size with Mn²⁺ addition was observed. This behavior is in good agreement with SEM analysis which showed a decrease in the grain size with Mn²⁺ addition. The increase in Mn²⁺ concentration reduces the concentration of zinc in the system leading to a decrease in diffusion rate in ZnO that could hinder the growth of the crystallite size in Mn²⁺-doped ZnO samples. A decrease in crystallite size in some Mn-doped ZnO systems was also reported in the literature data [44, 45].

**Fig. 7** Raman spectra of the 2% Mn²⁺-doped ZnO powder

Raman spectroscopy

Raman spectrum of the ZnO doped with 2% Mn sample is presented in Fig. 7. The peak at 435 cm⁻¹ can be assigned to the high-frequency branch of the E_2 mode of ZnO, e.g., the main Raman mode in the wurtzite crystal structure. This peak is sensitive to internal stress being related to motion of the oxygen atoms [46, 47]. According to full width at half maximum (FWHM) of 11 cm⁻¹ for the E_2^{High} mode, good crystal quality of the 2% Mn²⁺-doped ZnO powder is noticeable. Peaks within 546–564 cm⁻¹ and 567–582 cm⁻¹ ranges (see inset of Fig. 7) are assignable to A_1 (LO) and E_1 (LO) modes, while the peak at about 571 cm⁻¹ is sensitive to changes in the free carrier concentration [48]. The latter modes may be due to Zn-located interstitial. The 330 cm⁻¹ frequency is a second-order vibration mode resulted from the $E_2^{\text{high}} - E_2^{\text{low}}$ multiple scattering processes. Hence, shifting of the E_2^{high} and A_1 (LO) modes toward lower frequency shows a larger tensile stress in the crystal. This indicates an increased number of defects such as vacancies and interstitials that arose from Mn²⁺ substituted for Zn²⁺ in the ZnO matrix, which is named as an indicator of the Mn²⁺ incorporation into the ZnO matrix [49, 50].

The results of morphological and structural characterization of the oxide samples obtained by thermal treatment of the corresponding gels, at 500 °C, for 1 h, showed that in all cases nanopowders with wurtzite structures were obtained.

The presence of manganese in the Mn²⁺-doped ZnO powders was put in evidence by EDX investigation, and in the FTIR spectra the band that appears in all doped samples at 421 cm⁻¹ can also be assigned to formation of Mn–O–Zn bonds.

The calculated d -spacing, crystallite size D , lattice parameters (a , c), volume V of unit cell of pure ZnO and Mn²⁺-doped ZnO powders from XRD measurements indicate the substitution of Mn²⁺ (ionic radius 0.8 Å) for Zn²⁺ (ionic radius 0.74 Å) in the ZnO structure. These results were also confirmed by Raman measurements.

Conclusions

ZnO and Mn²⁺-doped ZnO-based gels and nanostructured powders were prepared by sol–gel method.

Mn²⁺-doped ZnO gels show a very similar thermal behavior with the undoped ZnO-based gel. Based on the TG/DTA results, the gels were thermally treated at 500 °C for 1 h, with a heating rate of 5 °C min⁻¹.

The resulted powders have ZnO hexagonal wurtzite structure, and in the case of Mn²⁺-doped ZnO samples, manganese ions have substituted zinc sites.

The mentioned results were sustained by all the methods of investigation used.

The structure and properties of the obtained powders recommend them as promising materials in potential piezoelectric applications.

Acknowledgements We gratefully acknowledge the support from the EU (ERDF) and Romanian Government that allowed for acquisition of the research infrastructure under POS-CCE O 2.2.1 project INFRANANOCHEM–No. 19/01.03.2009 and M-ERANET 12/2015 Piezoelectric MEMS for efficient energy harvesting–PiezoMEMS project.

References

- El Ghoul J, Barthou C, El Mir L. Synthesis, structural and optical properties of nanocrystalline vanadium doped zinc oxide aerogel. *Physica E*. 2012;44:1910–5.
- Khorsand Zak A, Abd. Majid WH, Abrishami ME, Yousefi R, Parvizi R. Synthesis, magnetic properties and X-ray analysis of Zn_{0.97}X_{0.03}O nanoparticles (X = Mn, Ni, and Co) using Scherrer and size–strain plot methods. *J Solid State Sci*. 2012;14:488–94.
- Li J, Fan H, Chen X, Cao Z. Structural and photoluminescence of Mn-doped ZnO single-crystalline nanorods grown via solvothermal method. *Colloids Surfaces A*. 2009;349:202.
- Ramesan MT, Jayakrishnan P, Sampreeth T, Pradyumnan PP. Temperature-dependent AC electrical conductivity, thermal stability and different DC conductivity modelling of novel poly(vinyl cinnamate)/zinc oxide nanocomposites. *J Therm Anal Calorim*. 2017;129:135–45.
- Firtat B, Moldovan C, Brasoveanu C, Muscalu G, Gartner M, Zaharescu M, Chesler P, Hornoiu C, Mihaiu S, Vladut C, Dascalu I, Georgescu V, Stan I. Miniaturised MOX based sensors for pollutant and explosive gases detection. *Sens Actuators B*. 2017;249:647–55.
- Rezkallah T, Djabri I, Koç MM, Erkovan M, Chumakov Y, Chemam F. Investigation of the electronic and magnetic properties of Mn doped ZnO using the FP-LAPW method. *Chin J Phys*. 2017;55:1432–40.
- Chen X, Jing X, Wang J, Liu J, Song D, Liu L. Fabrication of spindle-like ZnO architectures for highly sensitive gas sensors. *Superlattices Microstruct*. 2013;63:204–14.
- Achouri F, Corbel S, Balan L, Mozet K, Giroit E, Medjahdi G, Ben Said M, Ghrabi A, Schneider R. Porous Mn-doped ZnO nanoparticles for enhanced solar and visible light photocatalysis. *Mater Des*. 2016;101:309–16.
- Liau LCK, Huang JS. Energy-level variations of Cu-doped ZnO fabricated through sol–gel processing. *J Alloys Compd*. 2017;702:153–60.
- Straumal BB, Protasova SG, Mazilkin AA, Myatiev AA, Straumal PB, Schutz G, Goering E, Baretzky B. Ferromagnetic properties of the Mn-doped nanograined ZnO films. *J Appl Phys*. 2010;108:073923.
- Dhruvashi XX, Tanemura M, Shishodia PK. Ferromagnetism in sol–gel derived ZnO: Mn nanocrystalline thin films. *Adv Mater Lett*. 2016;7(2):116–22.
- Kolesnik S, Dabrowski B, Mais J. Origin of Spin-Glass Behavior of Zn_{1-x}Mn_xO. *J Supercond Nov Magn*. 2002;15:251–5.
- Meron T, Markovich G. Ferromagnetism in Colloidal Mn²⁺-Doped ZnO Nanocrystals. *J Phys Chem B*. 2005;109:20232–6.
- Fukumura T, Jin Z, Ohtomo A, Koinuma H, Kawasaki M. An oxide-diluted magnetic semiconductor: Mn-doped ZnO. *Appl Phys Lett*. 1999;75:3366–8.
- Sanz R, Jensen J, Gonzalez-Diaz G, Martinez O, Vazquez M, Hernandez-Velez M. Continuous and Localized Mn Implantation of ZnO. *Nanoscale Res Lett*. 2009;4:878–87.
- Cheng XM, Chien CL. Magnetic properties of epitaxial Mn-doped ZnO thin films. *J Appl Phys*. 2003;93:7876–8.
- Huang JCA, Hsu HS, Sun JH, Chiu SL, Lee CH, Liao YF, Chou H. Citation, Study of the local environment diversity between Co and Mn-doped ZnO single crystal film by multilayer growth technique. *J Appl Phys*. 2008;103:7.
- Jurca B, Tirsoaga A, Ianculescu A, Carp O. Influence of the synthesis parameters on the thermal behavior of some ZnO-starch composites. *J Therm Anal Calorim*. 2014;115:495–501.
- Murugadoss G. Synthesis and characterization of transition metals doped ZnO nanorods. *J Mater Sci Technol*. 2012;28:587–93.
- Sivalingam D, Gopalakrishnan JB, Rayappan JBB. Structural, morphological, electrical and vapour sensing properties of Mn doped nanostructured ZnO thin films. *Sens Actuators B: Chem*. 2012;166–167:624–31.
- Shankar DB, Alange RC, More SD, Murumkar VD, Jadhav KM. Sol–gel auto combustion synthesis, structural and magnetic properties of Mn doped ZnO nanoparticles. *Procedia Manuf*. 2018;20:174–80.
- Stefan M, Ghica D, Nistor SV, Maraloiu AV, Plugaru R. Mn²⁺ ions distribution in doped sol–gel deposited ZnO films. *Appl Surf Sci*. 2017;396:1880–9.
- Asmatulu R, Haynes H, Shinde M, Lin YH, Chen YY, Ho JC. Magnetic characterizations of sol–gel-produced Mn-doped ZnO. *J Nanomater*. 2010;2010:1–3.
- Dole BN, Mote VD, Huse VR, Purushotham Y, Lande MK, Jadhav KM, Shah SS. Structural studies of Mn doped ZnO nanoparticles. *Curr Appl Phys*. 2011;11:762–6.
- Jiang Y, Wang W, Jing C, Cao C, Chu J. Sol–gel synthesis, structure and magnetic properties of Mn-doped ZnO diluted magnetic semiconductors. *Mater Sci Eng, B*. 2011;176:1301–6.
- Sharma RK, Patel S, Pargaian KC. Synthesis, characterization and properties of Mn-doped ZnO nanocrystals. *Adv Nat Sci: Nanosci Nanotechnol*. 2012;3:1–5.
- Ali AG, Dejene FB, Swart HC. Effect of Mn doping on the structural and optical properties of sol–gel derived ZnO nanoparticles. *Cent Eur J Phys*. 2012;10:478–84.
- Abrishami ME, Kompany A, Hosseini SM, Ghajari Bardar N. Preparing undoped and Mn-doped ZnO nanoparticles: a comparison between sol–gel and gel-combustion methods. *J Sol–Gel Sci Technol*. 2012;62:153–9.
- Omri K, El Ghoul J, Lemine OM, Bououdina M, Zhang B, El Mir L. Magnetic and optical properties of manganese doped ZnO nanoparticles synthesized by sol–gel technique. *Superlattices Microstruct*. 2013;60:139–47.
- Omri K, Lemine OM, El Ghoul J, El Mir L. Sol–gel synthesis and room temperature ferromagnetism in Mn doped ZnO nanocrystals. *J Mater Sci: Mater Electron*. 2015;26:5930–6.

31. Mote VD, Purushotham Y, Dole BN. Structural, morphological, physical and dielectric properties of Mn doped ZnO nanocrystals synthesized by sol–gel method. *Mater Des.* 2016;96:99–105.
32. Panigrahy B, Aslam M, Bahadur D. Aqueous synthesis of Mn- and Co-doped ZnO nanorods. *J Phys Chem C.* 2010;114:11758–63.
33. Wang D, Park S, Lee Y, Eom T, Lee S, Lee Y, Choi C, Li J, Liu C. Epitaxial ZnMnO/ZnO coaxial nanocable. *Cryst Growth Des.* 2009;9:2124.
34. Djerdj I, Garnweitner G, Arocon D, Pregelj M, Jagličić Z, Niederberger M. Diluted magnetic semiconductors: Mn/Co doped ZnO nanorods as case study. *J Mater Chem.* 2008;18:5208–17.
35. Clavel G, Willinger MG, Zitoun D, Pinna N. Solvent dependent shape and magnetic properties of doped ZnO nanostructures. *Adv Funct Mater.* 2007;17:3159–69.
36. Mickovic Z, Alexander DTL, Sienkiewicz A, Mionic M, Forró L. Magrez a synthesis of nanosized Mn-doped ZnO by low temperature decomposition of hydrozincite precursors. *Cryst Growth Des.* 2010;10:4437–41.
37. Bilecka I, Luo L, Djerdj I, Rossell MD, Jagodič M, Jagličić Z, Masubuchi Y, Kikkawa S, Niederberger M microwave-assisted nonaqueous sol–gel chemistry for highly concentrated ZnO-based magnetic semiconductor nanocrystals. *J Phys Chem C.* 2011;115:1484–95.
38. Mihaiu S, Szilágyi IM, Atkinson I, Mocioiu OC, Hunyadi D, Pandelescu J, Toader A, Munteanu C, Boyadjiev S, Madarasz J, Pokol G, Zaharescu M. Thermal study on the synthesis of the doped ZnO to be used in TCO films. *J Therm Anal Calorim.* 2016;124:71–80.
39. Zaharescu M, Mocioiu OC, Chapter 9: Infrared Spectroscopy. In: T. Schneller, R. Waser, M. Kosec, D. Payne, editors. *Book: Chemical Solution Deposition of Functional Oxide Thin Films*, Ed. Springer: Wien; 2013. p. 213–230.
40. Parikh SJ, Chorover J. FT–IR study of biogenic Mn oxidation. *Geomicrobiol J.* 2005;22:207–18.
41. Moezzi A, McDonagh A, Dowd A, Cortie M. Zinc hydroxyacetate and its transformation to nanocrystalline zinc oxide. *Inorg Chem.* 2013;52:95–102.
42. Hossein Habibi M, Askari E. Synthesis of nanocrystalline zinc manganese oxide by thermal decomposition of new dinuclear manganese(III) precursors. *J Therm Anal Clorim.* 2013;111(2):1345–9.
43. Mote VD, Purushotham Y, Dole BN. Structural, morphological, physical and dielectric properties of Mn doped ZnO nanocrystals synthesized by sol–gel method. *Mater Des.* 2016;96:99–105.
44. Karmakar R, Neogi SK, Banerjee A, Bandyopadhyay S. Structural; morphological; optical and magnetic properties of Mn doped ferromagnetic ZnO thin film. *Appl Surf Sci.* 2012;263:671–7.
45. Senthilkumaar S, Rajendran K, Banerjee S, Chini TK, Sengodan V. Influence of Mn doping on the microstructure and optical property of ZnO. *Mater Sci Semicond Process.* 2008;11:6–12.
46. Cao B, Cai W, Zeng H, Duan G. Morphology evolution and photoluminescence properties of ZnO films electrochemically deposited on conductive glass substrates. *J App Phys.* 2006;99:073516–21.
47. Duan L, Rao G, Wang Y, Yu J, Wang T. Magnetization and Raman scattering studies of (Co, Mn) codoped ZnO nanoparticles. *J Appl Phys.* 2008;104:013909–13.
48. Huang Y, Liu M, Li Z, Zeng Y, Liu S. Raman spectroscopy study of ZnO-based ceramic films fabricated by novel sol–gel process. *Mater Sci Eng, B.* 2003;97:111–6.
49. Mavrin B, Demyanets L, Zakalukin R. Raman spectroscopy and Fermi resonance in Mn-doped ZnO bulk single crystal. *Phys Lett A.* 2010;374:4054–6.
50. Qing-Bo H, Jia-Yue X, Li X, Kamzin A, Kamzina L. Raman spectroscopy and magnetic properties of Mn-doped ZnO bulk single crystal. *Chin Phys Lett.* 2007;24:3499–501.